nature nanotechnology

SUPPLEMENTARY INFORMATION

DOI: 10.1038/NNANO.2014.209

Electrostatic control of thermoelectricity in molecular junctions

Youngsang Kim, Wonho Jeong, Kyeongtae Kim, Woochul Lee, and Pramod Reddy

Supplementary Information Contents:

© 2014 Macmillan Publishers Limited. All rights reserved.

1. Nanofabrication and preparation of samples

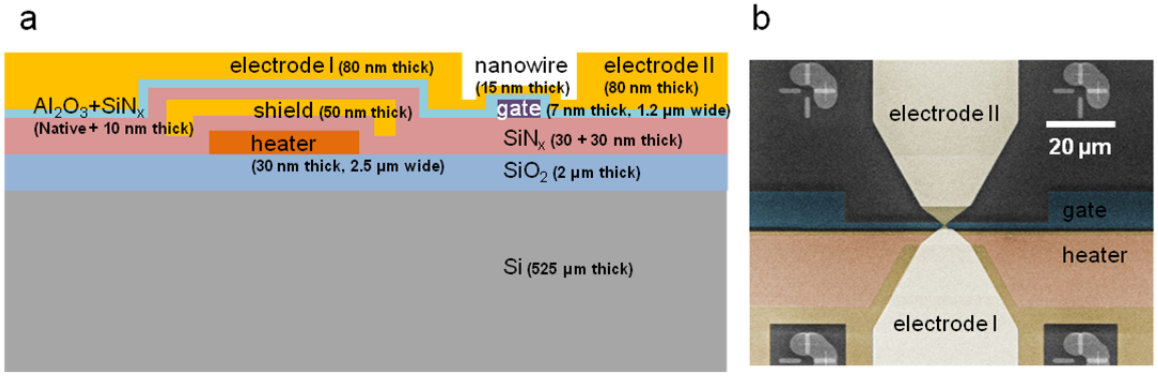

Figure S1| Schematic and a representative scanning electron microscope (SEM) image of EBJIH devices. *(**a**) Cross-sectional view (not drawn to scale and proportion) (**b**) SEM image of a nanofabricated EBJIH. The layers below the electrodes are created with low thermal conductivity materials to prevent parasitic heat transfer between the electrodes of MJs.*

The fabrication of the devices used in this work, electromigrated break junctions with integrated heater (EBJIHs, Fig. S1), involved multiple steps. We began by first lithographically defining an integrated heater (30 nm thick Au and 2.5 µm wide in the narrowest part, Fig. S1b) on a silicon (Si) wafer, which has a 2 µm thick low temperature silicon oxide (LTO) pre-deposited on top of it. We note that the LTO layer, which has a low thermal conductivity, serves to thermally isolate the heater from the underlying Si substrate, which is thermally much more conductive. Subsequently, we deposited a 30 nm thick layer of plasma enhanced chemical vapour deposition (PECVD) silicon nitride (SiN_x) on the entire wafer including the heater line. Further, a shield layer (50 nm thick Au) covering the integrated heater was lithographically defined: This shield layer, which is subsequently electrically grounded, ensures that the excitation signal supplied to the heater does not capacitively couple to other electrodes and electronic components. Subsequently, a 30 nm thick PECVD SiN_x layer was deposited on the shield layer to electrically isolate it from subsequent layers. Then, a thin Al gate (7 nm thick) was lithographically defined and oxidized, which was followed by a 10 nm thick PECVD SiN_x deposition. The gate electrode is chosen to be very thin so that its contribution to parasitic heat transfer between the hot and cold electrodes is minimised. Further, the 10 nm SiN_x layer serves to reduce parasitic heat loss from the hot to the cold sides. After this process, thin Au nanowires (15 nm thick, ~150 nm wide and 250 nm long) were defined by e-beam lithography and evaporation. Finally, thick Au electrodes (80 nm thick) were lithographically defined in order to ensure good electrical contact with Au nanowires and to provide electrical access to the device electrodes and the heater and

© 2014 Macmillan Publishers Limited. All rights reserved.

shield lines. Prior to starting the electromigration and other measurements using the nanofabricated samples, desired molecules of biphenyl-4,4'-dithiol (BPDT) or fullerene (C_{60}) were assembled on samples which were pre-cleaned by O_2 plasma (10 min at 250 mW). The prepared samples were immersed in a dilute solution of BPDT molecules (~0.1 mM) in 2 ml ethanol for >5 hours or a solution of C_{60} molecules (~0.1 mM) in 2 ml toluene for 2 minutes. Subsequently, the samples exposed to BPDT molecules were rinsed with ethanol and blown dry, whereas the samples covered by C_{60} molecules were dried without the rinse process[S1,2,3,4,5].

2. Verification of the presence of temperature differentials across nanometre-sized gaps

In order to confirm the existence of temperature differentials across nanogaps, we first performed finite element modelling using COMSOL (Joule heating module). An electric current was simulated through the integrated heater, while all other surfaces were considered to be electrically insulated. In addition, the temperature of the bottom surface (Si substrate), which is in contact with the cold-finger of the cryostat in our experiments, was modelled to be at 100 K, while all other surfaces were considered to be insulating. Further, the triangular shaped feature located on electrode I (Fig. S2a) was introduced to mimic the effect of the shield layer, which enhances heat transfer from the integrated heater to the nanogap (through electrode I).

The thermal conductivity was chosen to be 320 W/m·K[S6] and 160 W/m·K[S7] for thick and thin Au electrodes, respectively. The thermal conductivity of the Al gate layer was chosen to be 11.75 W/m·K[S8]. Further, the thermal conductivity of Si, SiO_2, SiN_x and Al_2O_3 were assigned to be 150 W/m·K[S6], 0.7 W/m·K[S9], 0.2 W/m·K[S9] and 1 W/m·K[S10], respectively. As can be seen in Fig. S2c, the calculated temperature profile shows a clear discontinuity at the nanogap and negligible temperature drop along Au electrodes. We note that in this modelling we ignored all thermal boundary resistances for computational simplicity. However, such thermal boundary resistances only serve to further increase the thermal resistance, which enhances the temperature drop across nanogap junctions. The mesh employed in our calculations is shown in Fig. S2d. It can be seen that the adaptive meshing scheme employed by us results in a relatively fine mesh (~10 nm) in the vicinity of the nanogap. The mesh size is in fact smaller than both the inelastic mean free path of electrons in the Au electrodes and the width of the nanowire in the device. Thus the finite element model provides an excellent continuum level description of the temperature field.

© 2014 Macmillan Publishers Limited. All rights reserved.

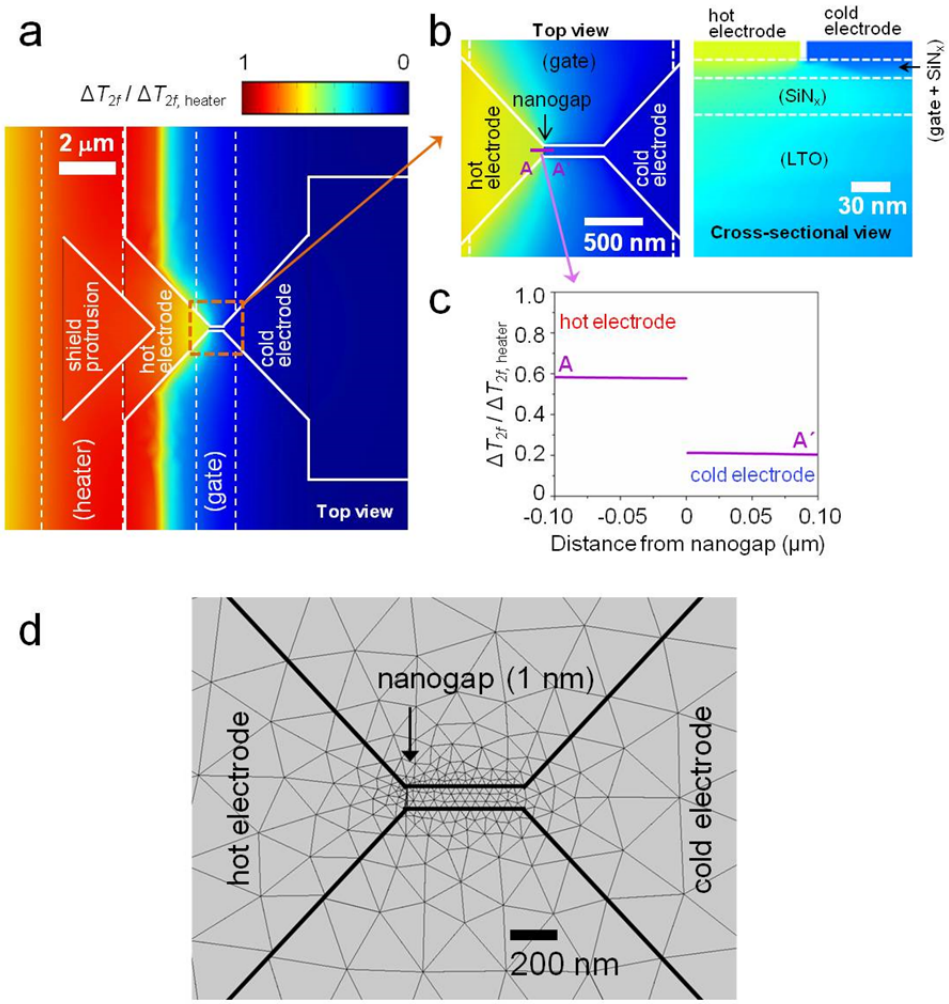

Figure S2| Modelled temperature fields in EBJIH devices. *(**a**) Calculated temperature fields of an EBJIH. The device including the nanowire is highlighted by solid lines for visual clarity. The embedded layers (gate, heater) are represented by dotted lines. (**b**) Magnified image of the region surrounding the nanogap indicated by the dotted square in (**a**). (**c**) Temperature profile along the line A-A' depicted in (**b**). The discontinuity of temperature amplitude at the nanogap is clearly seen. (**d**) Depiction of the mesh employed in our finite element modelling. There are no points within the nanogap as the surfaces surrounding the nanogap are assumed to be thermally insulating.*

We note that the results of the above calculation can be qualitatively understood as follows. From Fourier's law for heat conduction in isotropic materials it is clear that the gradient of the temperature field ($\vec{\nabla}T$) is related to the local heat flux ($\vec{q}$) and the thermal conductivity (k) via the following relationship: $\vec{\nabla}T = -\vec{q}/k$. This implies that the temperature gradients are large in the presence of large heat fluxes and/or low thermal conductivity. The finite element simulations

© 2014 Macmillan Publishers Limited. All rights reserved.

presented above indeed reflect this fact and show that the temperature gradients within the two electrodes that surround the nanogap (see Fig. 1b in the main manuscript) are small. This is because the heat currents in this region are relatively small and the thermal conductivity of Au is relatively large. Further, the simulations suggest that there is a significant temperature drop across the nanogap. In order to experimentally demonstrate the presence of a temperature drop across the nanogap, it is necessary to prove the following statements: 1) the temperature gradients in the electrodes surrounding the nanogap are small/negligible, 2) the temperature of the electrodes on the two sides of the nanogap is different. To elaborate, if the above statements are proven we would know that there is a negligible temperature drop within each electrode and that there is a temperature differential between the electrodes implying that the temperature drop has to be in the nanogap.

We unambiguously established the presence of a temperature differential and estimated the actual temperature drop across nanogaps by measuring temperature fields in the vicinity of the nanogap (as shown in Fig. 1 of the manuscript) using ultra-high vacuum scanning thermal microscopy (UHV-SThM)[S11,12]. The amplitude of temperature oscillations of the heater and the amplitude of the temperature differential across the nanogap were measured while applying AC power to the heater (Fig. S3a). As expected, the amplitude of temperature oscillations of the heater and the nanogap show a linear dependence on the power input to the heater. In order to map the amplitude of temperature oscillations with high spatial resolution we measured temperature amplitude along nanowires at neighbouring points separated by ~8 nm from each other. The data from one such measurement is shown in Fig. S3b and clearly shows an abrupt temperature drop across the nanogap. The result also shows that the temperature gradients within the electrodes are very small. Hence, it is expected that the temperature at the edge of the electrodes is the same as the temperature of a point that is within each electrode and ~8 nm away from it. Thus the experimental results unambiguously confirm that there is a temperature differential across the nanogap.

We performed similar measurements on six different devices (three line scans like the one shown in Fig. S3b on each device). Based on these measurements we estimated the average temperature amplitude of the hot and cold electrodes. From these data the temperature drop across the nanogap (more precisely the difference in the amplitude of temperature oscillations) was

© 2014 Macmillan Publishers Limited. All rights reserved.

estimated to be ~34 ± 3% of the amplitude of temperature oscillations of the heater ($\Delta T_{2f,\ \text{heater}}$, which represents the hottest part of the device) as summarised in Table S1. We note that these temperature fields remain unperturbed even when molecules are incorporated into the gap as the thermal resistance of molecular junction is extremely large (>10^{10} K/W)[S13,14,15].

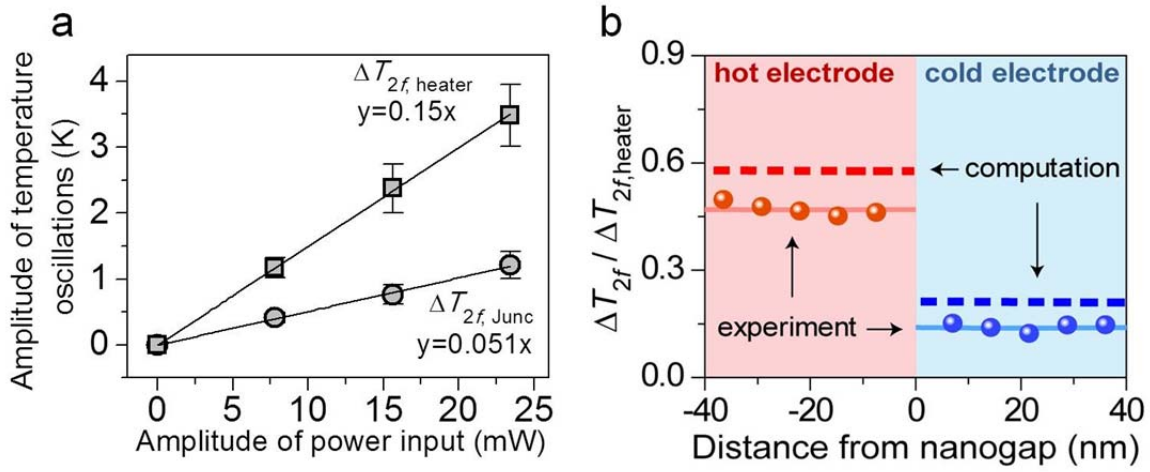

Figure S3| Characterisation of temperature fields in the vicinity of the nanogap in EBJIH devices. *(**a**) Measured amplitude of temperature oscillations of the heater (square symbols) and the measured amplitude of the temperature differential across the nanogap (circles) are shown as a function of the amplitude of power input to the integrated heater. The obtained linear relationship is used to estimate the appropriate power input required to establish 1 K, 2 K, 3 K and 4 K temperature differentials across nanogaps during thermoelectric voltage measurements. (**b**) Presence of the temperature differentials across nanogaps was confirmed by UHV-SThM, which shows that the drop in the amplitude of temperature oscillations across the nanogap is ~34% of the amplitude of temperature oscillations of the heater. Circles: measured temperature amplitude along nanowires, Solid lines: linear fits to the experimental data, and Dotted lines: calculated temperature profile from Figs. S2b and S2c.*

Table S1| Summary of the measured temperature differentials across nanogaps. *The amplitude of temperature oscillations of the heater* ($\Delta T_{2f,\ \text{heater}}$) *was assigned to be 1, and all other temperature amplitude oscillations were normalised accordingly.*

	Devices					
	#1	#2	#3	#4	#5	#6
Hot electrode	0.64	0.59	0.64	0.67	0.55	0.62
Cold electrode	0.25	0.27	0.29	0.32	0.24	0.28
$\Delta T_{2f,\ \text{Junc}}$ (% of $\Delta T_{2f,\ \text{heater}}$)	39	32	35	35	31	34

© 2014 Macmillan Publishers Limited. All rights reserved.

3. Thermoelectric voltage measurements and estimation of the Seebeck coefficient of MJs

3.1. Thermoelectric voltage measurements

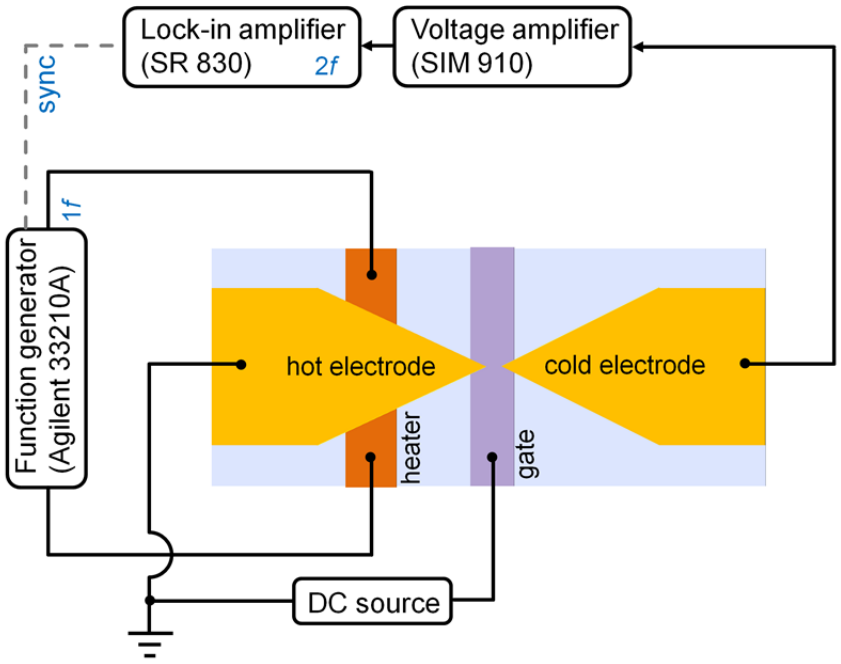

Figure S4| Schematic of the thermoelectric voltage measurement setup.

In order to establish temperature differentials across the nanogap junction, we apply a sinusoidal electric current to the integrated heater at a frequency f = 5 Hz using a function generator (Agilent 33210A), and resulting in temperature differentials that oscillate at $2f$ (Fig. S4). This in turn results in thermoelectric voltage differentials across the junction. The thermoelectric voltage differentials are measured by first buffering the signals using a high input impedance (100 MΩ) voltage amplifier (SIM 910) and subsequently measuring using a SR 830 lock-in amplifier (LIA) in a bandwidth of 0.078 Hz. While measuring the thermoelectric voltages of MJs, the gate voltage was incremented in steps of 2 V with a 10 sec delay between the steps to minimise the effects of capacitive coupling between the gate electrode and other electrodes of MJs. At each gate voltage step, the output of the LIA was recorded for one second and averaged to obtain one data point. This was repeated ten times to get ten data points at each step. The data shown in the manuscript is the average of ten data points whereas the error bars represent the standard deviation of these data. For the gate voltage dependent low-bias conductance measurements, the same measurement scheme was used to estimate the average and the standard deviation. The

© 2014 Macmillan Publishers Limited. All rights reserved.

applied gate voltage was restricted to be in the range of ±8 V as the ~12 nm thick dielectric layer (native Al_2O_3 + SiN_x) between the Al gate electrode and the Au electrodes of MJs was found to break down at gate voltages of ~±10 V. In section 3.3 we provide a detailed discussion of how we determined the sign of the Seebeck coefficient of MJs.

3.2. Stability of the nanogap and the frequency dependence of thermoelectric voltages

As described in the main manuscript, all Seebeck coefficient data were obtained under applied modulated temperature differentials. One may suspect that the temperature modulations may result in periodic thermal expansion and contraction of the gap, which may be detrimental to the stability of the junction and result in measurement artefacts. In order to rule out this concern, we experimentally quantified the magnitude of the change in gap size and found it to be negligibly small. To establish this fact, we first created vacuum tunnel junctions by electromigration[S12] of our devices. For such tunnel junctions the low-bias conductance (G) is given, to an excellent approximation[S2,16,17] by $G(d) = Ae^{-\beta d}$, where A is a constant, β is the attenuation factor (~1.85 Å^{-1} for vacuum tunnel junctions[S16]) and d is the gap size. This implies that if a small DC bias is applied the resulting tunnelling current is given by $I_{DC} = G(d)V_{DC}$. Further, under such a bias, if the gap size is modulated sinusoidally (i.e., by the thermal expansion effect) at a frequency $2f$ by an amplitude $\Delta d << d$, a sinusoidal current with an amplitude given by $I_{2f} = [\beta G(d)\Delta d]V_{DC}$ is also set up due to the modulation of the low-bias conductance. From these relationships it can be seen that

$$I_{2f} / I_{DC} = \beta \Delta d . \quad \text{(S1)}$$

Therefore, the modulation in gap size (Δd) can be obtained by measuring I_{DC}, I_{2f} and from knowledge of β. In Fig. S5a we show the scheme employed by us to quantify the effect of applied temperature modulations on the gap size. Specifically, we applied small DC biases across the electrodes while applying a sinusoidal temperature modulation of ~1 K at a frequency $2f$ (10 Hz) across the gap. The measured values of I_{DC} and I_{2f} under these conditions are shown in Fig. S5b. As expected and in accordance with the aforementioned relationships, in the small bias limit both the AC and DC components increase linearly. Further, the fact that I_{2f} increases linearly with the applied bias eliminates the possibility that it is a thermoelectric current arising

© 2014 Macmillan Publishers Limited. All rights reserved.

from the applied temperature differential. From Fig. S5b, it can be seen that I_{2f} / I_{DC} ~0.02. Therefore, from equation (S1) (and β ~1.85 Å^{-1}) it can be seen that Δd is ~1.1 pm. This implies that the change in gap size is ~1.1 pm/K. We also note that such displacements are comparable to the amplitude of thermally excited vibrations of Au atoms at 100 K[S18,19]. Under such small gap modulations we found that the low-bias conductance of the molecular junctions is extremely stable showing that the electronic structure and the energy levels of the junctions are unaffected.

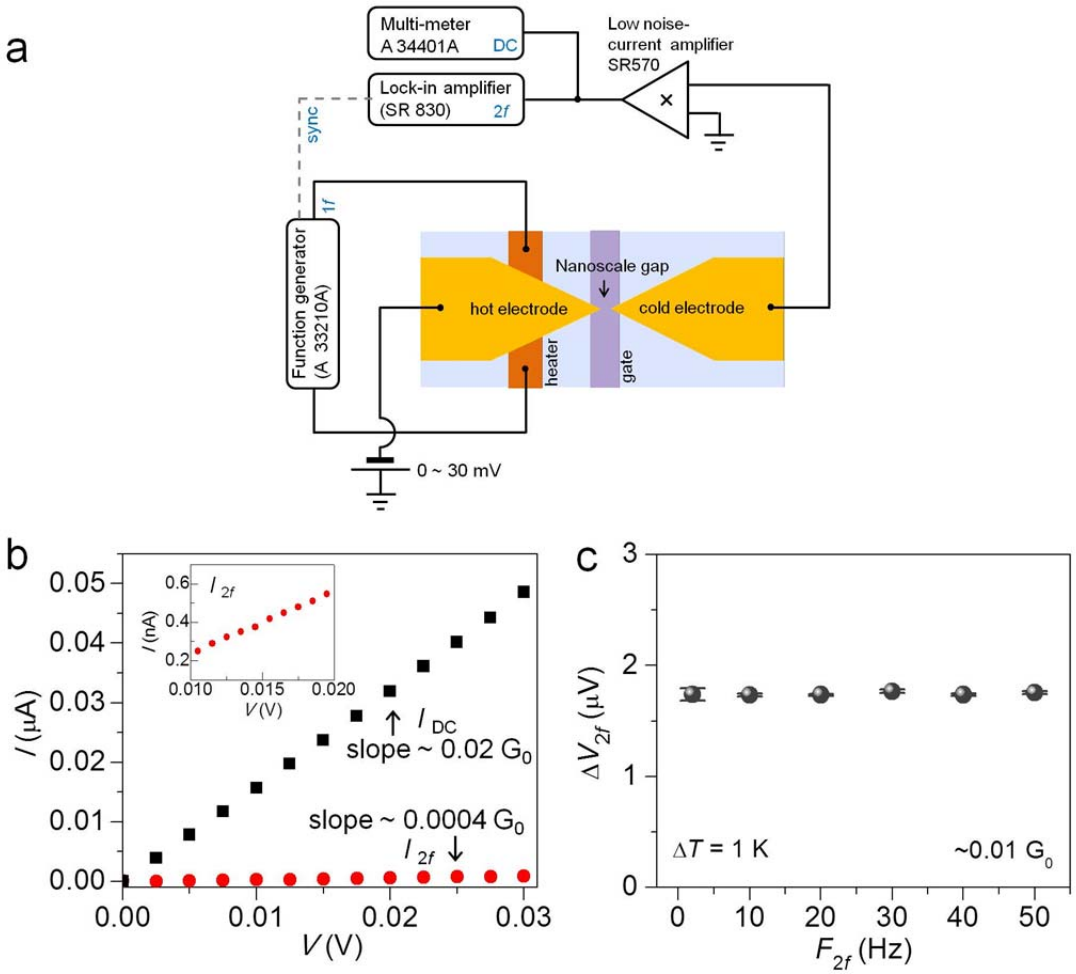

Figure S5| Quantification of the stability of nanogaps and the frequency dependence of thermoelectric voltages. *(**a**) Schematic of the experimental setup for quantifying amplitude of thermally induced expansion. (**b**) DC tunnelling current (I_{DC}, black squares) and 2f component of the tunnelling current (I_{2f}, red circles) resulting from modulation of the gap size due to thermal expansion were measured as a function of the DC bias (V_{DC}) applied to a tunnel junction. The inset shows the magnified view of I_{2f}. It can be seen that I_{2f} is ~2% of I_{DC} indicating that the displacement of nanogap by the oscillating thermal expansion is ~1.1 pm/K. (**c**) Frequency independent thermoelectric voltages (ΔV_{2f}) of a tunnel gap (G ~0.01 G_0). ΔV_{2f} is independent of the frequency (2f) until 50 Hz.*

© 2014 Macmillan Publishers Limited. All rights reserved.

In order to further confirm that the experimental result is indeed reasonable, we computed the change in gap size using finite element modelling. Specifically, we used the known geometry of the devices (i.e., the thickness and dimensions of the layers) in conjunction with known thermal expansion coefficients of the materials in the device to estimate the displacement of gap size for a 1 nm sized tunnel junction (the expected gap size of our junctions). From this modelling, we found that the gap size changes by ~1.6 pm per Kelvin temperature differential across the nanogap, which is in excellent agreement with our experimental estimate. Therefore, based on the above two independent estimates we conclude that the changes in gap size are <8 pm even for the largest temperature differentials applied in our measurements (4 K). Such small changes in gap size are known to negligibly impact the thermoelectric properties of molecular junctions.

In addition, we tested the frequency independence of thermoelectric voltages (ΔV_{2f}) in a tunnel gap as shown in Fig. S5c. It can be seen that the measured ΔV_{2f} is indeed independent of the frequency even when the frequency ($2f$) is raised to 50 Hz, which is 5 times larger than the temperature modulation frequency of our experiments. This result shows that there is indeed no capacitive coupling between higher harmonics of the sinusoidal voltage bias applied to the heater and the voltage output across the electrodes.

3.3. Determination of the sign of the Seebeck coefficient

Information regarding the sign of the Seebeck coefficient is contained in the phase of the thermoelectric voltage output. We begin by noting that if thermoelectric voltage measurements are performed by applying unmodulated (DC) temperature differentials, the sign of the Seebeck coefficient of MJs can be easily obtained by knowing whether the hot electrode is at a higher or lower electrical potential with respect to the cold electrode. However, such a DC measurement scheme suffers from a low signal to noise ratio and makes it difficult to perform measurements under small temperature differentials, which are required to prevent temperature related instabilities in MJs. Whereas, the AC measurement scheme adapted in our experiments enables a high signal to noise ratio and makes possible the measurement of thermoelectric voltages even with small temperature differentials (1 K – 4 K). Here we describe how the sign of the Seebeck coefficient of MJs can be extracted by monitoring the phase of the thermoelectric voltage output.

© 2014 Macmillan Publishers Limited. All rights reserved.

When a sinusoidal current $I = I_0 \sin(\omega t)$ at a frequency $\omega = 2\pi f$ is applied to the heater, the power dissipation is given by:

$$P = I^2 R = I_0^2 R \sin^2(\omega t) = \frac{I_0^2 R}{2}\left[1 - \cos(2\omega t)\right] = \frac{I_0^2 R}{2}\left[1 + \sin\left(2\omega t - \frac{\pi}{2}\right)\right] \quad \text{(S2)}$$

This implies that if a sinusoidal reference signal at 2ω is created from the excitation signal such that the nodes of the reference signal are coincident with the alternating nodes of the excitation signal, i.e., if the reference signal is given by (as is generated by the digital signal processor in LIA):

$$I = I_0 \sin(2\omega t) \quad \text{(S3)}$$

then there is a phase delay of –90° between the internally generated reference signal and the heat dissipation of the system. The temperature fields of EBJIHs are proportional to the power dissipation with an additional phase delay (ϕ), which is a small value and reflects the thermal characteristics of the devices. Thus, the oscillating temperature fields are given by:

$$T(t) = \Delta T_{2f,\text{heater}}\left[1 + \sin\left(2\omega t - \left(\frac{\pi}{2} + \phi\right)\right)\right] \quad \text{(S4)}$$

where $\Delta T_{2f,\text{ heater}}$ is the amplitude of temperature oscillations of the heater. We note that the position dependence of ϕ is very weak for the modulation frequency used in the experiments, and hence there is no measurable phase difference between two neighbouring points that are separated by a few nanometres. Therefore, the 2ω component of temperature oscillations across the junction is given by:

$$\Delta T_{2f,\text{Junc}} = \Delta T_{2f,\text{Hot}} - \Delta T_{2f,\text{Cold}} = \Delta T_{2f,\text{Junc}} \sin\left(2\omega t - \left(\frac{\pi}{2} + \tilde{\phi}\right)\right) \quad \text{(S5)}$$

Finally, the thermoelectric voltage output is given by:

$$\Delta V_{2f} = -S_{\text{Junc}} \Delta T_{2f,\text{Junc}} \quad \text{(S6)}$$

© 2014 Macmillan Publishers Limited. All rights reserved.

Further, it can be seen that:

$$\left.\begin{aligned}\Delta V_{2f} &= S_{\text{Junc}}\Delta T_{2f,\text{Junc}}\sin\left(2\omega t+\left(\frac{\pi}{2}-\tilde{\phi}\right)\right) \text{ when } S_{\text{Junc}} \text{ is positive}\\ \Delta V_{2f} &= S_{\text{Junc}}\Delta T_{2f,\text{Junc}}\sin\left(2\omega t-\left(\frac{\pi}{2}+\tilde{\phi}\right)\right) \text{ when } S_{\text{Junc}} \text{ is negative}\end{aligned}\right\} \quad \text{(S7)}$$

From equation (S7), it is clear that if the sign of the Seebeck coefficient changes, then the phase of thermoelectric voltages changes accordingly. Therefore, we can conclude that when the measured phase difference, with respect to the reference signal is ~–90° the Seebeck coefficient is negative, and when the measured phase difference is ~+90° the Seebeck coefficient is positive. In addition, the sign of the Seebeck coefficient was also checked by applying a large DC power to the heater and measuring the DC thermoelectric voltages between the electrodes of MJs using a DC voltmeter and was found to be consistent with that obtained from the phase information.

3.4. Effect of thermal gradients in other parts of the device on the measured S_{Junc}

The Seebeck coefficient is defined by the following relation,

$$\Delta V = -S\Delta T \quad \text{(S8)}$$

Thus, we can show that,

$$\begin{aligned}&V_2-V_1=-S_{\text{bk}}(T_2-T_1), \qquad V_3-V_2=-S_{\text{tk}}(T_3-T_2),\\ &V_4-V_3=-S_{\text{tn}}(T_4-T_3), \qquad V_5-V_4=-S_{\text{Junc}}(T_5-T_4),\\ &V_6-V_5=-S_{\text{tn}}(T_6-T_5), \qquad V_7-V_6=-S_{\text{tk}}(T_7-T_6), \qquad V_8-V_7=-S_{\text{bk}}(T_8-T_7)\end{aligned} \quad \text{(S9)}$$

where S_{Junc} is the Seebeck coefficient of the molecular junction, S_{bk} is the Seebeck coefficient of bulk Au, S_{tk} is the Seebeck coefficient of ~80 nm thick Au thin-film, S_{tn} is the Seebeck coefficient of ~15 nm thick Au thin-film, V_x and T_x are the amplitude of voltage oscillations and the amplitude of temperature oscillations at each of the points (x = 1–8), respectively.

© 2014 Macmillan Publishers Limited. All rights reserved.

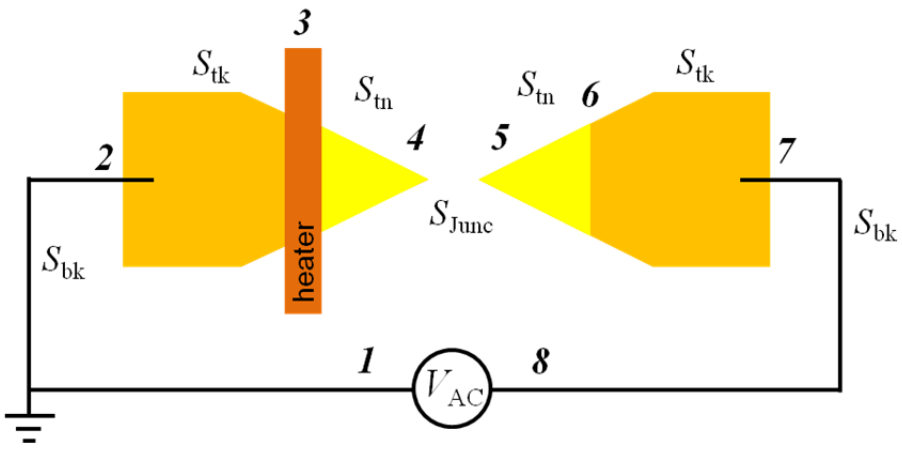

Figure S6| Schematic diagram labelling various portions of the EBJIH where temperature differentials are present. *The Seebeck coefficients of the various portions of the device are labelled by S_{bk}, S_{tk}, S_{tn} and S_{Junc} and indicate the Seebeck coefficient of bulk Au, ~80 nm thick Au thin-film, ~15 nm thick Au thin-film and the molecular junction, respectively.*

We consider the Seebeck coefficient of two different thin-films separately because it is expected that their Seebeck coefficients are slightly different. We also note that in our device the amplitude of temperature oscillations at locations 1, 2, 7 and 8 is negligible. After adding the seven equations in (S9) we get,

$$V_8 - V_1 = (S_{tk} - S_{tn})(T_6 - T_3) + (S_{tn} - S_{Junc})(T_5 - T_4) \tag{S10}$$

$$S_{Junc} = -\frac{V_8 - V_1}{T_5 - T_4} + S_{tn} + \frac{T_6 - T_3}{T_5 - T_4}(S_{tk} - S_{tn}) \tag{S11}$$

We note that,

$$V_8 - V_1 = \Delta V_{2f}\ ,\quad T_5 - T_4 = \Delta T_{2f,\,Junc} \quad \text{and} \quad \frac{T_6 - T_3}{T_5 - T_4} \approx 3 \tag{S12}$$

The last term in (S12) is ascertained from both our thermal modelling and SThM measurements. From equation (S11) and (S12), it is clear that the Seebeck coefficient of the junction is given by,

$$S_{Junc} = -\frac{\Delta V_{2f}}{\Delta T_{2f,\,Junc}} + S_{tk} + 2(S_{tk} - S_{tn}) \tag{S13}$$

© 2014 Macmillan Publishers Limited. All rights reserved.

Therefore, in order to obtain S_{Junc} it is necessary to incorporate the Seebeck coefficient of both ~80 nm and ~15 nm thick Au thin-films (S_{tk} and S_{tn}). It is known that the Seebeck coefficient of bulk Au is ~2 μV/K[S20,21] at room temperature (300 K) and decreases to ~0.8 μV/K[S22] at 100 K because the Seebeck coefficient is approximately linearly proportional to the ambient temperature. Further, we note that the Seebeck coefficient of Au thin-films show only small deviations from that of bulk Au[S21], and the difference of the Seebeck coefficient between ~80 nm and ~15 nm thick Au thin-films is also small[S21]. Therefore, the last term of equation (S13), $S_{\text{tk}} - S_{\text{tn}}$, is equal to zero to a very good approximation. Thus S_{Junc} is given by:

$$S_{\text{Junc}} = -\frac{\Delta V_{2f}}{\Delta T_{2f,\,\text{Junc}}} + S_{\text{tk}} \qquad \text{(S14)}$$

where S_{tk} is ~0.8 μV/K[S22] and was used in estimating the Seebeck coefficient of molecular junctions in this work.

3.5. Examples of the linear fit of thermoelectric voltages vs. temperature differentials

As described briefly in the manuscript, the Seebeck coefficient was obtained by plotting ΔV_{2f} vs. $\Delta T_{2f,\,\text{Junc}}$ and then computing the Seebeck coefficient from equation (S14). In Fig. S7, we show representative plots for Au-BPDT-Au and Au-C_{60}-Au junctions obtained when no gate voltage was applied ($V_{\text{G}} = 0$ V).

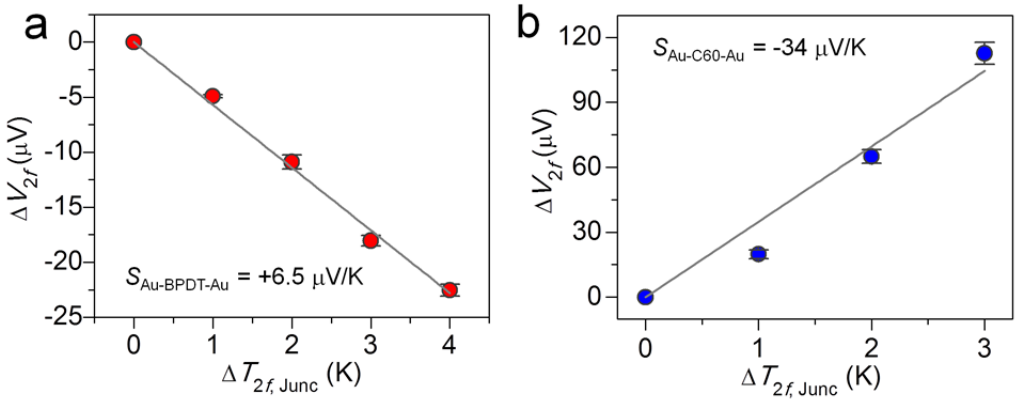

Figure S7| Examples of linear fits to the measured thermoelectric voltage data. *Representative linear fits of ΔV_{2f} vs. $\Delta T_{2f,\,\text{Junc}}$ used to obtain the Seebeck coefficient of BPDT (**a**) and C_{60} (**b**) junctions at $V_{\text{G}} = 0$ V. These sets of data are obtained from the data shown in Fig. 2b and 3b of the manuscript.*

© 2014 Macmillan Publishers Limited. All rights reserved.

4. Variability in the measured low-bias conductance and Seebeck coefficient of junctions

Creation of molecular junctions in EBJIHs is a stochastic process, therefore not all electromigrated junctions have molecules bridging the electrodes. In our experiments, a total of 1152 devices were nanofabricated, of which 464 devices (~40%) were found to be suitable for use in our experiments. The remaining had defects such as gate leakage and failure of nanowires by electrostatic discharge. Among these, after electromigration at 100 K, ~35% (162/464) displayed non-trivial *I-V* characteristics. However, only a much smaller subset (~3% (14/464), seven for BPDT junctions and seven for C_{60} junctions) had repeatable characteristics (low-bias conductance and Seebeck coefficient) and could be operated reliably to obtain the full-set of data from diverse measurements during a couple of hours. All these junctions showed a non-trivial dependence of the low-bias conductance and the Seebeck coefficient on the gate voltage. This low-yield is indeed consistent with that observed in previous works[S23,24,25]. In our experiments, junctions that show Coulomb-blockade effect[S5,25] were not considered as such characteristics may arise from Au clusters embedded between the electrodes or weak coupling of the molecules to the electrodes among other reasons. Further, since the microscopic details of the molecular junctions created by electromigration are not controllable, the low-bias conductance and the Seebeck coefficient measured in our experiments show a broad distribution. In Fig. S8, we show the variability in the measured low-bias conductance and the Seebeck coefficient when no gate voltage is applied. The average of the measured low-bias conductance values of Au-BPDT-Au junctions is ~10 times larger than that of a single molecular junction (~0.001 G_0)[S2,26,27,28], which may attributed to the presence of multiple molecules in the junctions. In contrast, the measured Seebeck coefficient of the junction is comparable to what is expected from previous measurements at ~300 K[S29,30]. This is due to the relative insensitivity of the measured Seebeck coefficient[S29,31] to the number of molecules in the junctions. The measured low-bias conductance values of C_{60} junctions are comparable to that of a C_{60} single molecular junction (~0.1 G_0)[S32,33] suggesting that only one or a few C_{60} molecules are present in the junctions. Further, the measured Seebeck coefficients of C_{60} junctions also fall into the range expected from the previous measurements at ~300 K[S33,34].

© 2014 Macmillan Publishers Limited. All rights reserved.

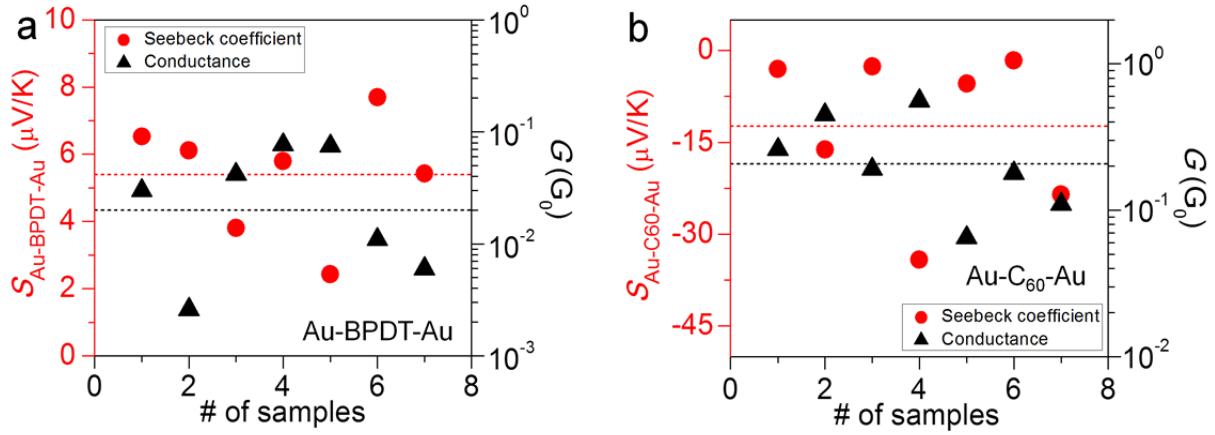

Figure S8| Variability in the measured low-bias conductance and the Seebeck coefficient of molecular junctions. *The low-bias conductance (G) and the Seebeck coefficient (S) of BPDT (**a**) and C_{60} (**b**) junctions when V_G = 0 V. Average values of S and G are ~+5.4 μV/K and ~0.02 G_0 for BPDT junctions and ~ –12.4 μV/K and ~0.2 G_0 for C_{60} junctions, respectively.*

5. Additional datasets of gated Seebeck coefficient measurements

In Fig. S9, we show two additional datasets of gated Seebeck coefficient of BPDT and C_{60} junctions (measured at 100 K). The Seebeck coefficient of BPDT junctions (Fig. S9a and S9b) is found to systematically decrease when the gate voltage is varied from –8 V to +8 V as the dominant HOMO level shifts away from E_F. Further, the Seebeck coefficient of these junctions were found to be ~+6 μV/K when no gate voltage was applied (V_G = 0 V). These values are very similar to that reported in the manuscript and reflect the relative insensitivity of the Seebeck coefficient of Au-BPDT-Au junctions to variations in junction geometry.

The measured Seebeck coefficient of two additional C_{60} junctions is shown in Fig. S9c and S9d, which feature a negative Seebeck coefficient (consistent with the data shown in the manuscript) that indicates charge transport is indeed LUMO dominanted[S33,35,36,37]. However, the gate dependence of the Seebeck coefficient of these junctions is different from each other and also different from what was shown in the manuscript. This is primarily due to the fact that in C_{60} junctions charge transport is very close to resonance, and hence the gate voltage dependence of the Seebeck coefficient is very sensitive to small perturbations in junction geometry (see discussion in section 7 for more details).

© 2014 Macmillan Publishers Limited. All rights reserved.

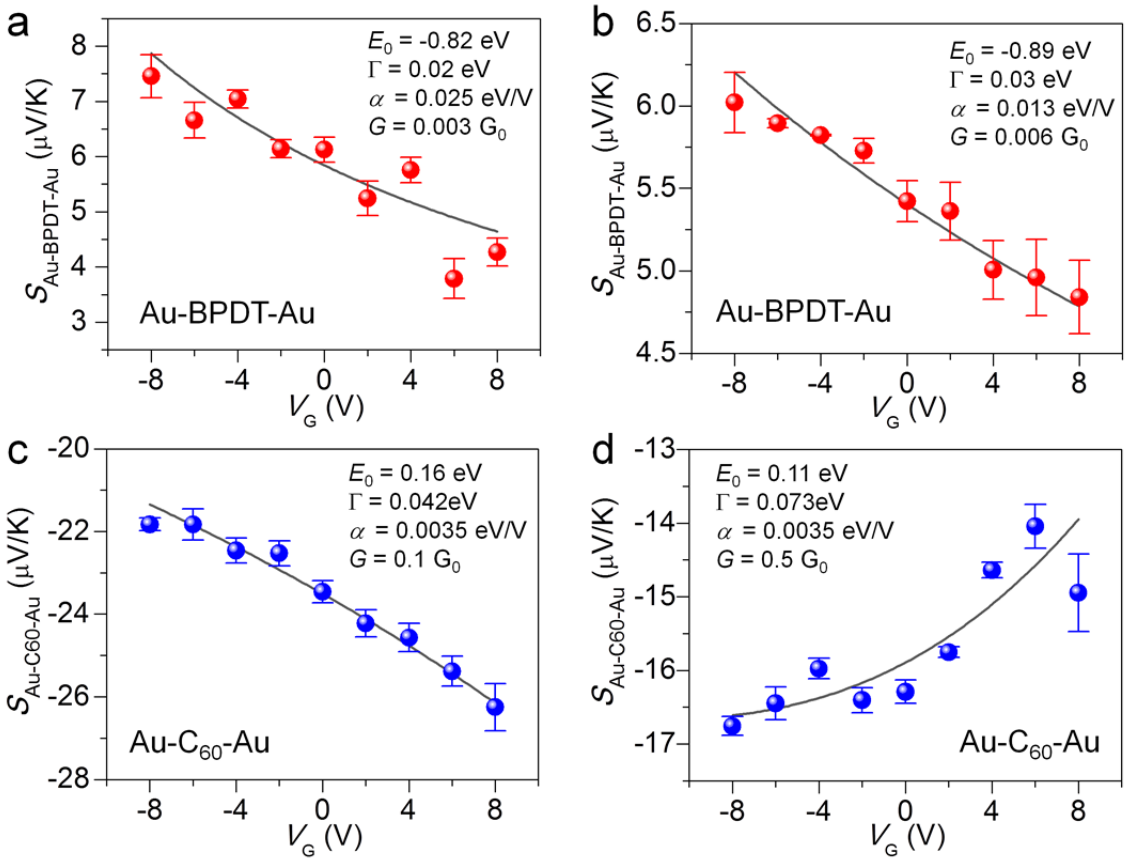

Figure S9| Additional datasets for gated Seebeck coefficient measurements. *The gated Seebeck coefficients are presented with curve fits obtained using equation (S16) for BPDT (**a**, **b**) and C_{60} (**c**, **d**) junctions. The values of fitting parameters are listed in the insets.*

6. Description of the one-level model employed to quantify the gate voltage dependence

The one-level model for charge transport has been extensively used to obtain additional insight into charge transport in MJs[S31,38]. In this work, we employed this model to obtain information about the electrode-molecule coupling and the energy level alignment relative to the chemical potential E_F. In the one-level model, the transmission function is given by the expression shown in equation (S15). The transmission function (T) and low bias conductance (G) depend on the energetic location of the molecular level (E_0), the coupling constant (Γ, in the case of symmetric coupling) as well as the gate voltage V_G[S31,39] and are given by:

$$T(E,V_G)=\frac{4\Gamma^2}{\left[E-(E_0-\alpha V_G)\right]^2+4\Gamma^2}\ ,\quad G=\frac{2e^2}{h}T\left(E=E_F,V_G\right) \qquad \text{(S15)}$$

The Seebeck coefficient of the junction can be related to the transmission by:

© 2014 Macmillan Publishers Limited. All rights reserved.

$$S_{\mathrm{Junc}}(V_{\mathrm{G}}) = -\frac{\pi^2 k_{\mathrm{B}}^2 T_{\mathrm{amb}}}{3|e|}\left.\frac{\partial \ln\left[T(E,V_{\mathrm{G}})\right]}{\partial E}\right|_{E=E_{\mathrm{F}}} = \frac{\pi^2 k_{\mathrm{B}}^2 T_{\mathrm{amb}}}{3|e|}\frac{2\left[E_{\mathrm{F}}-\left(E_0-\alpha V_{\mathrm{G}}\right)\right]}{\left[E_{\mathrm{F}}-\left(E_0-\alpha V_{\mathrm{G}}\right)\right]^2+4\Gamma^2} \qquad \text{(S16)}$$

where k_{B} is the Boltzmann constant, e is the charge of an electron, and T_{amb} is the ambient temperature.

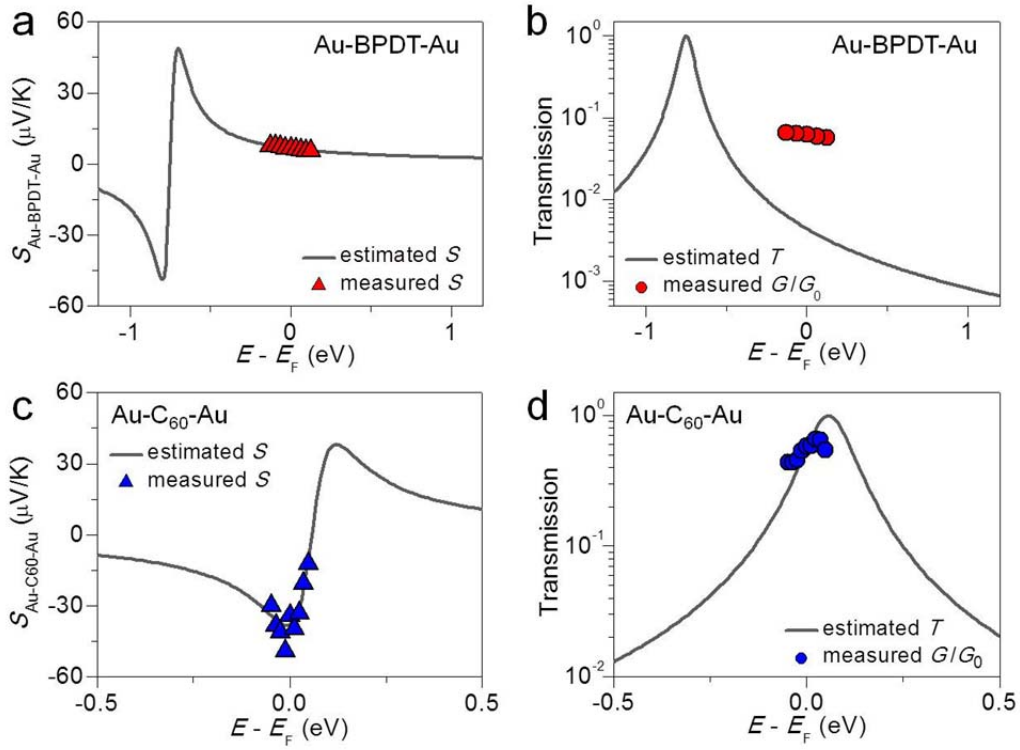

Figure S10| Alternative presentation of data for visualising the effect of gate voltages on the thermoelectric properties of molecular junctions. *The Seebeck coefficient and transmission corresponding to the parameters obtained by fitting the one-level transport model to the Seebeck coefficient data shown in Figs. 2 and 3 of the main manuscript. Experimental data (symbols) for the BPDT junction are shown in (**a**, **b**) and data for the C_{60} junction are shown in (**c**, **d**). The parameters corresponding to the one-level model are: Γ = 0.025 eV, E_0 = –0.75 eV, α = 0.016 eV/V for the BPDT junction and Γ = 0.032 eV, E_0 = +0.057 eV, α = 0.006 eV/V for the C_{60} junction.*

In the main manuscript, we analysed the shift in the energetic separation between the resonant energy level and E_{F} when gate voltages are applied. Specifically, these shifts were obtained by fitting the measured Seebeck coefficients to the equation (S16). Here, we present the same data in a slightly different form in Fig. S10. In plotting these figures we assume that the position of the dominant transport orbital is fixed and the position of the chemical potential changes. This

© 2014 Macmillan Publishers Limited. All rights reserved.

approach has been used by several researchers including in a recent work[S40] and is presented here for the sake of completeness.

It can be seen from Fig. S10a and S10c that the measured Seebeck coefficients fit the one-level model very well. Further, in correspondence to what has been discussed in the main manuscript, it can be seen in Fig. S10b that the measured low-bias conductance is larger than that predicted by the model. This can be directly attributed to the presence of multiple molecules in the junction. We note again that we fit the experimental data to equation (S16) because the Seebeck coefficient is insensitive to the number of molecules in the junction.

7. Additional discussion of the gate voltage dependence of the Seebeck coefficient in Au-C_{60}-Au Junctions

In order to understand the gate voltage dependence of the Seebeck coefficient of C_{60} junctions, we show in Fig. S11a the transmission in a scenario where transport is close to resonance: i.e., the peak of the transmission function is close to E_F. We plot the transmission using the same parameters that were extracted for the Au-C_{60}-Au junction in the manuscript: $\Gamma = 0.032$ eV, $E_0 = +0.057$ eV, $\alpha = 0.006$ eV/V and $V_G = 0$. Further, in Fig. S11b we show the computed Seebeck coefficient (using equation (S16) and the transmission in Fig. S11a) as the position of transmission peak (E_0) is varied with respect to E_F. Here we note that the equation (S16) was simplified in the low temperature limit. However, we found from calculations[S31], performed without making the low temperature approximation, that the Seebeck coefficient does not differ significantly from that obtained using equation (S16). It can be seen that from Fig. S11 that when $\Delta = E_F - E_0 = 0$, i.e., when the peak is aligned with E_F, the Seebeck coefficient becomes zero. Further, it is clear that when $\Delta = -0.062$ eV the magnitude of the Seebeck coefficient is the largest. This existence of a valley at $\Delta = -0.062$ eV is due to a sign change in the curvature ($\kappa \propto \partial^2 T / \partial E^2$) of the transmission at the point where the blue and red regions meet in Fig. S11a (the inflection point marked by the arrow). Therefore, it is clear that if transport is close to resonance a non-monotonic change in the magnitude of the Seebeck coefficient can be observed.

© 2014 Macmillan Publishers Limited. All rights reserved.

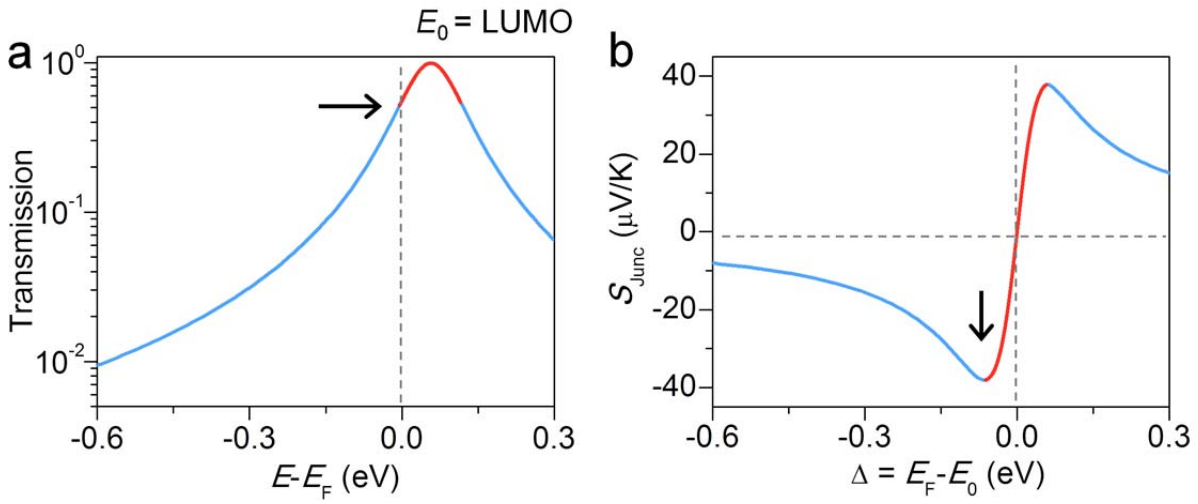

Figure S11| Interpretation of the U-shaped feature observed in the gate dependent Seebeck coefficient data of Au-C_{60}-Au junction. *Example of a transmission curve for a Au-C_{60}-Au junction (**a**) and the corresponding Seebeck coefficient computed using equation (S16) (**b**). The arrow in (**a**) indicates the position of an inflection point. The regions of the curve shown in different colours have different signs of curvature. In (**b**) the Seebeck coefficient is plotted as a function of $\Delta = E_F - E_0$ (as E_0 is varied with respect to E_F) to visualise the sign change of the Seebeck coefficient and the "U" shaped feature similar to that reported in the manuscript.*

8. Gate voltage independence of the low-bias conductance and the Seebeck coefficient in junctions created from pristine devices

We performed control experiments on pristine devices that were not exposed to molecules. Upon electromigration of these devices we create a vacuum gap between the electrodes of the device. We studied the gate voltage dependence of the low-bias conductance and the Seebeck coefficient of such vacuum tunnel junctions. The results obtained from these measurements on two representative devices, one with a large low-bias conductance (~0.46 G_0) and the other with a smaller low-bias conductance (~0.006 G_0) are shown in Fig. S12. It can be seen that both the low-bias conductance and the Seebeck coefficient are independent of the applied gate voltage—in strong contrast to what is seen in Au-BPDT-Au and Au-C_{60}-Au junctions described in the manuscript. In addition, the magnitude of the Seebeck coefficient of these vacuum tunnel junctions is seen to be significantly smaller than what was measured on molecular junctions. Finally, the sign of the Seebeck coefficient is found to be negative in both cases indicating LUMO-like tunnelling.

© 2014 Macmillan Publishers Limited. All rights reserved.

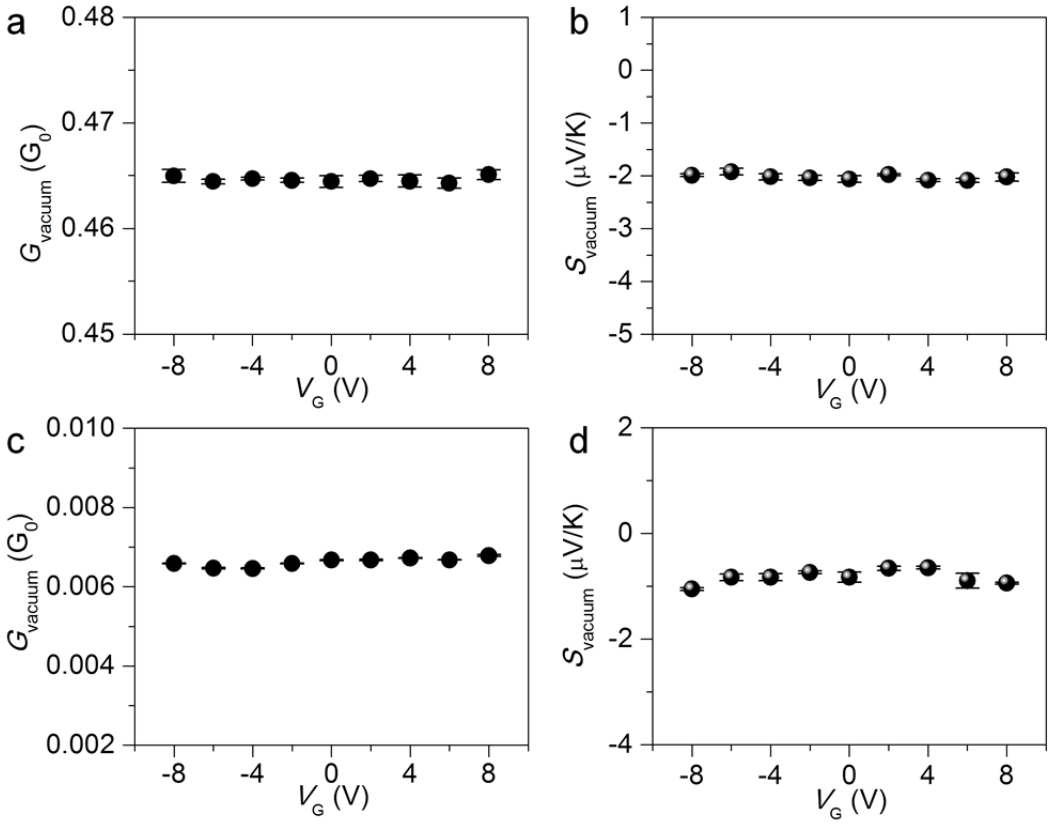

Figure S12| Gate voltage independence of the electrical conductance and the Seebeck coefficient of vacuum tunnel junctions. *Low-bias conductance (**a**, **c**) and Seebeck coefficient (**b**, **d**) as a function of gate voltage for electromigrated EBJIHs that were not exposed to molecules. The Seebeck coefficient shown in (**b**) and (**d**) were measured on the same junctions corresponding to the data shown in (**a**) and (**c**), respectively.*

9. Inelastic electron tunnelling spectroscopy (IETS)

We employed IETS (d^2I/dV^2) to identify the unique vibrational modes of Au-BPDT-Au and Au-C_{60}-Au junctions. These spectra provide additional evidence confirming the presence of appropriate molecules in the nanogaps of EBJIHs[S1,23,41,42,43,44]. In Fig. S13, IETS spectra obtained by numerical computation from *I*-*V* curves (measured at 100 K)[S43,44,45,46] are presented. The red curves in Fig. S13 represent antisymmetrised spectra (*AS*), obtained by $AS = (f(V) - f(-V)) / 2$, where $f(V)$ represents the IETS data. The similarity between the IETS spectra and the *AS* confirms that molecules are almost symmetrically bonded to both electrodes. In addition, the fact that peaks appear at the same absolute voltages for both bias polarities provides strong evidence that they indeed originate from molecular vibrations[S32,42,47]. Therefore, we assign the vibrational modes, which appear in both bias polarities symmetrically.

© 2014 Macmillan Publishers Limited. All rights reserved.

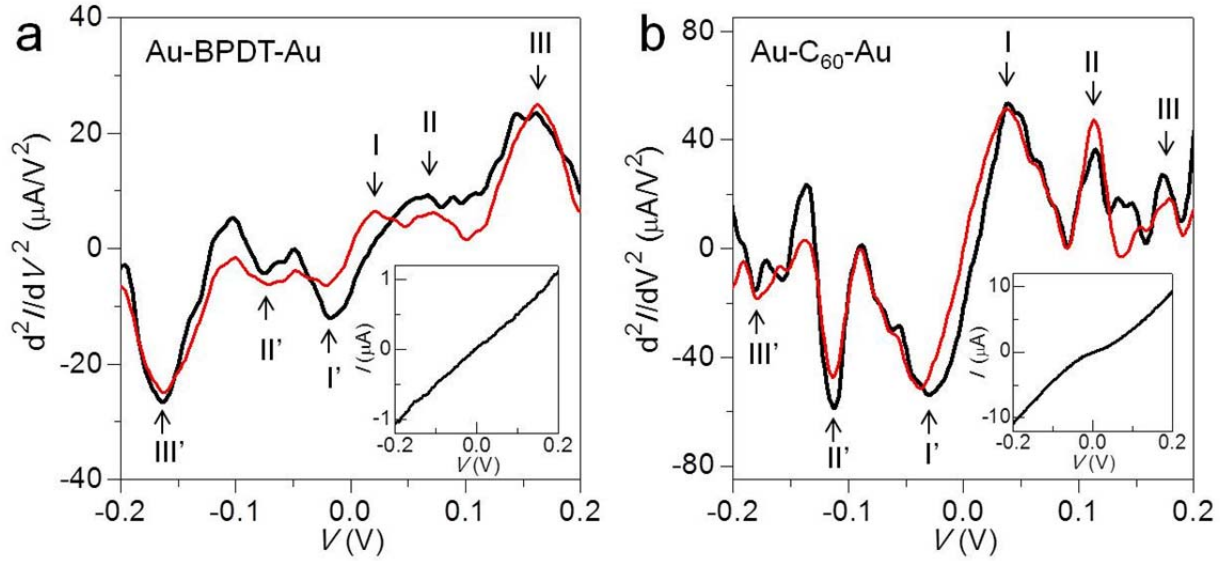

Figure S13| Inelastic electron tunnelling spectra of molecular junctions. *IETS spectra and I-V curves (inset) corresponding to the same (**a**) Au-BPDT-Au and (**b**) Au-C_{60}-Au junctions on which we made thermoelectric measurements. IETS spectra (black) for both bias polarities are shown together with a curve antisymmetrised (red) with respect to the bias polarity, obtained by the simple formula, AS = (f(x) – f(–x)) / 2. IETS spectra were obtained from numerical derivative of each I-V curve in the inset. Roman numerals in (**a**) and (**b**) indicate each vibrational mode as listed in the Table S2 and S3 for BPDT and C_{60} junctions, respectively.*

We note that the IETS spectrum obtained at 100 K is significantly broadened and hence only a few peaks can be detected[S48]. This is evident in the IETS data presented in Fig. S13. Although the peaks are not sharp, they provide compelling evidence for the presence of the appropriate molecules in the Au-BPDT-Au and Au-C_{60}-Au junctions. The molecular vibrational modes corresponding to the peaks are listed in Table S2 and S3.

Table S2| Summary of the vibrational mode assignment in the IETS spectra of a Au-BPDT-Au junction. *The identified peak positions in the IETS spectra are in good agreement with previous theoretical calculations and experiments listed in the references below.*

Peak position (mV)		Mode	Description	References
I	20	ν(Au-S)	Au-S stretching	S23, S43
II	70	ν(C-S)	C-S stretching	S1, S46, S48, S49
III	160	γ(C-H)	C-H in-plain bending	S1, S46, S48, S49

© 2014 Macmillan Publishers Limited. All rights reserved.

Table S3| Summary of the vibrational mode assignment in the IETS spectra of a Au-C_{60}-Au junction. *The identified peak positions in the IETS spectra are in good agreement with previous theoretical calculations and experiments listed in the references below.*

Peak position (mV)		Modes	References
I	39	Gu(1) / Hg(1/2)	S32, S50, S51
II	112	Gg(4) / Hg(4)	S32, S52
III	180	Hg(7)	S50, S51

© 2014 Macmillan Publishers Limited. All rights reserved.

References

S1. Kim, Y., Pietsch, T., Erbe, A., Belzig, W. & Scheer, E. Benzenedithiol: A broad-range single-channel molecular conductor. *Nano Lett.* **11**, 3734-3738 (2011).

S2. Song, H., Kim, Y., Jeong, H., Reed, M. A. & Lee, T. Intrinsic charge transport of conjugated organic molecules in electromigrated nanogap junctions. *J. Appl. Phys.* **109**, 102419 (2011).

S3. Kim, Y. *et al.* Charge transport characteristics of diarylethene photoswitching single-molecule junctions. *Nano Lett.* **12**, 3736-3742 (2012).

S4. Yu, L. H. & Natelson, D. The Kondo effect in C_{60} single-molecule transistors. *Nano Lett.* **4**, 79-83 (2004).

S5. Park, H. *et al.* Nanomechanical oscillations in a single-C_{60} transistor. *Nature* **407**, 57-60 (2000).

S6. Haynes, W. M. *CRC handbook of chemistry and physics*. 94th edn, (CRC Press, 2013).

S7. Chen, G. & Hui, P. Thermal conductivities of evaporated gold films on silicon and glass. *Appl. Phys. Lett.* **74**, 2942 (1999).

S8. Roh, H. H. *et al.* Novel nanoscale thermal property imaging technique: The 2ω method. II. Demonstration and comparison. *J. Vac. Sci. Technol. B* **24**, 2405 (2006).

S9. Lee, S.-M. & Cahill, D. G. Heat transport in thin dielectric films. *J. Appl. Phys.* **81**, 2590 (1997).

S10. Lee, S.-M., Cahill, D. G. & Allen, T. H. Thermal conductivity of sputtered oxide films. *Phys. Rev. B* **52**, 253 (1995).

S11. Kim, K., Jeong, W., Lee, W. & Reddy, P. Ultra-high vacuum scanning thermal microscopy for nanometer resolution quantitative thermometry. *ACS Nano* **6**, 4248-4257 (2012).

S12. Jeong, W., Kim, K., Kim, Y., Lee, W. & Reddy, P. Characterizaion of nanoscale temperature fields during electromigration of nanowires. *Sci. Rep.* **4**, 4975 (2014).

S13. Segal, D., Nitzan, A. & Hänggi, P. Thermal conductance through molecular wires *J. Chem. Phys.* **119**, 6840 (2003).

S14. Losego, M. D., Grady, M. E., Sottos, N. R., Cahill, D. G. & Braun, P. V. Effects of chemical bonding on heat transport across interfaces. *Nature Mater.* **11**, 502-506 (2012).

S15. Wang, R. Y., Segalman, R. A. & Majumdar, A. Room temperature thermal conductance of alkanedithiol self-assembled monolayers *Appl. Phys. Lett.* **89**, 173113 (2006).

S16. Ward, D. R., Huser, F., Pauly, F., Cuevas, J. C. & Natelson, D. Optical rectification and field enhancement in a plasmonic nanogap. *Nature Nanotech.* **5**, 732-736 (2010).

S17. Choi, S. H., Kim, B. & Frisbie, C. D. Electrical resistance of long conjugated molecular wires. *Science* **320**, 1482-1486 (2008).

S18. Fitzsimmons, M. R., Burkel, E. & Sass, S. L. Experimental measurement of the thermal displacive properties of a large-angle twist grain boundary in gold. *Phys. Rev. Lett.* **61**, 2237-2240 (1988).

S19. Cartz, L. Thermal vibrations of atoms in cubic crystals II: The amplitude of atomic vibrations. *Proc. Phys. Soc. B* **68**, 957 (1955).

S20. Kasap, S. O. *Principles of electronic materials and devices*. 2nd edn, (McGraw-Hill, 2002).

S21. Lin, S. L. & Leonard, W. F. Thermoelectric power of thin gold films. *J. Appl. Phys.* **42**, 3634-3639 (1971).

S22. Rowe, D. M. *CRC Handbook of Thermoelectrics*. (CRC Press, 1995).

S23. Song, H. *et al.* Observation of molecular orbital gating. *Nature* **462**, 1039-1043 (2009).

© 2014 Macmillan Publishers Limited. All rights reserved.

S24. Yoshida, K. *et al.* Gate-tunable large negative tunnel magnetoresistance in Ni-C_{60}-Ni single molecule transistors. *Nano Lett.* **13**, 481-485 (2013).
S25. Osorio, E. A. *et al.* Addition energies and vibrational fine structure measured in electromigrated single-molecule junctions based on an oligophenylenevinylene derivative. *Adv. Mater.* **19**, 281-285 (2007).
S26. Dell, E. J. *et al.* Impact of molecular symmetry on single-molecule conductance. *J. Am. Chem. Soc.* **135**, 11724-11727 (2013).
S27. Malen, J. A. *et al.* Identifying the length dependence of orbital alignment and contact coupling in molecular heterojunctions. *Nano Lett.* **9**, 1164-1169 (2009).
S28. Guo, S. Y., Zhou, G. & Tao, N. J. Single molecule conductance, thermopower, and transition voltage. *Nano Lett.* **13**, 4326-4332 (2013).
S29. Reddy, P., Jang, S. Y., Segalman, R. A. & Majumdar, A. Thermoelectricity in molecular junctions. *Science* **315**, 1568-1571 (2007).
S30. Malen, J. A. *et al.* The nature of transport variations in molecular heterojunction electronics. *Nano Lett.* **9**, 3406-3412 (2009).
S31. Cuevas, J. C. & Scheer, E. *Molecular electronics : an introduction to theory and experiment*. (World Scientific, 2010).
S32. Böhler, T., Edtbauer, A. & Scheer, E. Conductance of individual C_{60} molecules measured with controllable gold electrodes. *Phys. Rev. B* **76**, 125432 (2007).
S33. Evangeli, C. *et al.* Engineering the thermopower of C_{60} molecular junctions. *Nano Lett.* **13**, 2141-2145 (2013).
S34. Yee, S. K., Malen, J. A., Majumdar, A. & Segalman, R. A. Thermoelectricity in fullerene-metal heterojunctions. *Nano Lett.* **11**, 4089-4094 (2011).
S35. Bilan, S., Zotti, L. A. & Cuevas, J. C. Theoretical study of the charge transport through C_{60}-based single-molecule junctions. *Phys. Rev. B* **85**, 205403 (2012).
S36. Géranton, G., Seiler, C., Bagrets, A., Venkataraman, L. & Evers, F. Transport properties of individual C_{60}-molecules. *J. Chem. Phys.* **139**, 234701 (2013).
S37. Ulstrup, S., Frederiksen, T. & Brandbyge, M. Nonequilibrium electron-vibration coupling and conductance fluctuations in a C_{60} junction. *Phys. Rev. B* **86**, 245417 (2012).
S38. Datta, S. *Electronic transport in mesoscopic systems*. (Cambridge University Press, 1995).
S39. Zotti, L. A. *et al.* Revealing the role of anchoring groups in the electrical conduction through single-molecule junctions. *Small* **6**, 1529-1535 (2010).
S40. Capozzi, B. *et al.* Tunable charge transport in single-molecule junctions via electrolytic gating. *Nano Lett.* **14**, 1400-1404 (2014).
S41. Troisi, A. & Ratner, M. A. Propensity rules for inelastic electron tunneling spectroscopy of single-molecule transport junctions. *J. Chem. Phys.* **125**, 214709 (2006).
S42. Kim, Y. *et al.* Charge transport in azobenzene-based single-molecule junctions. *Phys. Rev. Lett.* **109**, 226801 (2012).
S43. Bruot, C., Hihath, J. & Tao, N. J. Mechanically controlled molecular orbital alignment in single molecule junctions. *Nature Nanotech.* **7**, 35 (2012).
S44. Tsutsui, M. & Taniguchi, M. Vibrational spectroscopy of single-molecule junctions by direct current measurements. *J. Appl. Phys.* **113**, 084301 (2013).
S45. Smit, R. H. M. *et al.* Measurement of the conductance of a hydrogen molecule. *Nature* **419**, 906-909 (2002).
S46. Hihath, J. *et al.* Inelastic Transport and Low-Bias Rectification in a Single-Molecule Diode. *ACS Nano* **5**, 8331-8339 (2011).

© 2014 Macmillan Publishers Limited. All rights reserved.

S47. Kim, Y., Hellmuth, T. J., Bürkle, M., Pauly, F. & Scheer, E. Characteristics of amine-ended and thiol-ended alkane single-molecule junctions revealed by inelastic electron tunneling spectroscopy. *ACS Nano* **5**, 4104-4111 (2011).
S48. Taniguchi, M., Tsutsui, M., Yokota, K. & Kawai, T. Inelastic electron tunneling spectroscopy of single-molecule junctions using a mechanically controllable break junction. *Nanotechnology* **20**, 434008 (2009).
S49. Sergueev, N., Roubtsov, D. & Guo, H. Ab Initio analysis of electron-phonon coupling in molecular devices. *Phys. Rev. Lett.* **95**, 146803 (2005).
S50. Sergueev, N., Demkov, A. A. & Guo, H. Inelastic resonant tunneling in C_{60} molecular junctions. *Phys. Rev. B* **75**, 233418 (2007).
S51. Franke, K. J., Schulze, G. & Pascual, J. I. Excitation of Jahn-Teller active modes during electron transport through single C60 molecules on metal surfaces. *J. Phys. Chem. Lett.* **1**, 500-504 (2010).
S52. Fock, J. *et al.* A statistical approach to inelastic electron tunneling spectroscopy on fullerene-terminated molecules. *Phys. Chem. Chem. Phys.* **13**, 14325-14332 (2011).

© 2014 Macmillan Publishers Limited. All rights reserved.